Engineering Ultralow Pd-content on CuO_X/C for Efficient Oxygen Reduction Electrocatalysis

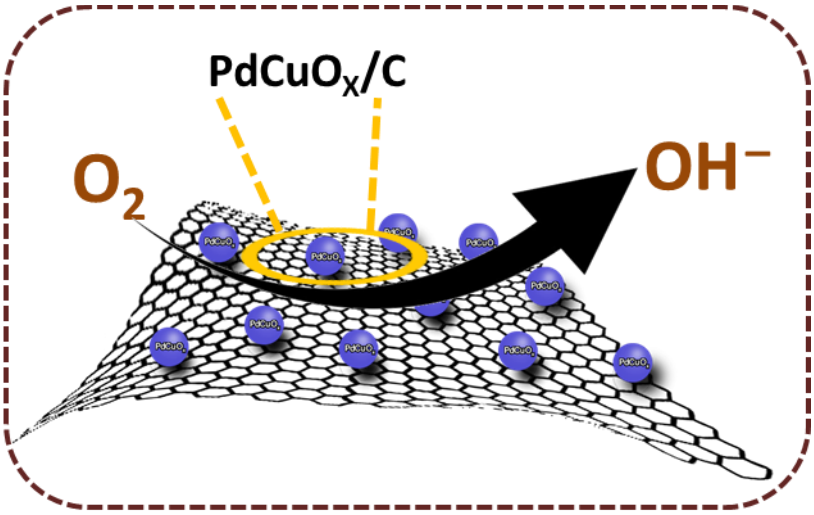

This Chapter describes the synthesis of an ultralow Pd-loaded non-precious transition metal oxide supported on graphene ($PdCuO_X/C$). The resultant electrocatalyst was evaluated for ORR in 0.1 M KOH. The $PdCuO_X/C$ electrocatalyst is highly active towards ORR compared to its CuO_X/C, $PdCuO_X$ and CuO_X counterparts. Additionally, it displays higher onset potential, larger ECSA and superior durability. The remarkable activity and durability of the $PdCuO_X/C$ are ascribed to the synergistic effects between $PdCuO_X$ and carbon support. Also, CuO_X tailors the electronic structure of Pd simultaneously to decrease the loading amount of Pd. This work represents a promising route to design ultralow noble metals-based electrocatalysts for energy conversion devices. The experimental methods for the synthesis, characterization techniques and electrocatalytic activity were covered in Chapter 2.

6.1. Introduction

In earlier chapters, we have covered the role of Pd and its significance as a possible Pt replacement for ORR. This is primarily due to Pd and Pt's have identical electronic characteristics, which mainly explain their outstanding ORR activity [1-3]. Although the average price of Pd was considerably lower compared to that of Pt, it is still more expensive than the other transition metals. Research has focused on mixing Pd with other transition metals to tune the electronic properties, lower the cost of Pd-based electrocatalysts, and boost their ORR activity [1-3]. Transition metal oxides (TMO) catalysts are effective electrocatalysts for energy conversion and storage technologies such as fuel cells (FCs). The ability of TMOs to mix effectively into a single material and have varied oxidation states are two of their special properties that improved the ORR performance [4-6]. TMOs are also highly abundant and inexpensive, making them a viable option for use as electrocatalysts in ORR because of their high availability and low cost. Copper oxides (CuO_X) are frequently employed choice among TMOs in various electrochemical reactions because of their large accessible surface area, different oxidation states, chemical stability, more abundance and environmentally benign nature [7-10]. However, its low catalytic performance and relatively weak conductivity prevent it from finding broad use. In the previous chapters, we have already discussed the physical characteristics of graphene and their role as a conductive support. Besides enhancing the conductivity of the material, the graphene support can disperse the nanoparticles (NPs) and expose more active sites [12, 13]. Furthermore, it has been employed as an anchoring site for loading metal NPs, resulting in SMSI and enhancing the charge transfer [11-13]. It is reported that metal-metal oxide heterojunctions have attracted a lot of attention because they enhance the intrinsic electrocatalytic activity of the material by enabling charge transfer and allowing the electron densities of different redox active sites to remain at the interface [14-20]. For instance, Choi *et al.* synthesized Pd–Mn_3O_4 by via polyol reduction of $Pd(acac)_2$ (0.70 mmol), 1,2-hexadecandiol (2.45 mmol) and $Mn_2(CO)_{10}$ (0.12 mmol). The ADT data shows that Pd–Mn_3O_4 exhibits the highest durability, 149% in MA and 142% in specific activity (SA) than the Pd/C [17]. Sahoo and coworkers prepared Pd-Fe_2O_3/NGO-CNT by mixing $PdCl_2$ (13.34 mg Pd), $FeCl_2.6H_2O$ (6.66 mg Fe), NRGO (60 mg), and CNTs (20 mg) and explored the activity towards ORR [18]. Liu and coworkers reported the synthesis of Pd_3Cu_1/N-rGO by taking 100 mg of N-rGO, 10 mM H_2PdCl_4 and 25 mM $CuCl_2$ solutions via a typical

hydrothermal strategy in one of their studies. The catalyst exhibited improved ORR activity and electrostability compared to benchmark Pt/C [19]. In another work, Zheng *et al.* prepared Cu_xPd_y nanocrystals by using 0.1 mmol of $Pd(acac)_2$, 0.3 mmol of $Cu(acac)_2$, 5 mL of oleylamine (OLA), and 4 mL of triethylene glycol and then supported on graphene to form G–Cu_xPd_y nanocomposites. Electrochemical analysis shows that the obtained G–Cu_3Pd NCPs show superior durability over conventional Pt/C catalyst [20]. Inspired by these above works, here we have developed graphene supported $PdCuO_X$ in which the content of Pd is 1000 times lower than CuO_X (also lesser loading (0.0056g of Pd in 20% metal ratio) than the previous chapters) and explore their performance toward ORR. We observe that $PdCuO_X/C$ exhibit enhanced ORR performance than the CuO_X/C in alkaline electrolytes. This work introduces a facile method to produce ultralow Pd loaded electrocatalysts (0.00005 mol) for ORR which are highly effective and cost-effective.

6.2. Results and discussion

6.2.1. Characterizations of the catalysts

The crystalline phases and structural property of $PdCuO_X/C$, CuO_X/C, $PdCuO_X$ and CuO_X were characterized by PXRD as shown in Figure 6.1a. The diffractions observed at 29.8°, 36.7°, 42.6°, 61.5°, 73.7° and 75.8° attributed to the lattice planes of (110), (111), (200), (220), (311) and (222) cubic Cu_2O, respectively [21, 22]. Similarly, the peaks observed at 32.5°, 38.9°, 53.5°, 66.3°, and 68.4°, which matches well with (110), (200), (020), (310) and (220) planes of monoclinic CuO [23, 24]. On the other hand, the appearance of the diffraction peak at 16.37° and 23.7° belong to the (020), (021) facets in all the samples have been assigned to the $Cu(OH)_2$ [25]. A characteristic peak of Cu at 50.44 indexed to (200) plane appeared in the XRD pattern indicating the presence of Cu NPs [9, 26]. Meanwhile, no characteristic diffraction peaks of Pd are observed in the XRD pattern due to small amount of Pd loading. Additionally, in $PdCuO_X/C$ and CuO_X/C hybrid NPs a peak was observed at a 2θ value of ~26°, which indexed to the (002) facet of the graphene.

The Raman spectra of CuO_X/C, $PdCuO_X/C$, $PdCuO_X$ and CuO_X are presented in Figure 6.1b. The Raman spectrum of CuO_X/C NPs shows peaks at 146, 216, 416, 527 and 626 cm^{-1} corresponding to Cu_2O. And the peaks at 302, 614 cm^{-1} correspond to the A_g and B_g mode of CuO [27-30]. It is worth noticing that these characteristic peaks of Cu_2O

and CuO of $PdCuO_X/C$ shifted to higher wavenumber values compared to that of CuO_X/C, which demonstrates the incorporation of Pd changes the bonding environment, being in line with XRD analysis. The noticeable two peaks of graphene is observed at around ~1356 and ~1575 cm^{-1}, which are associated with the disordered sp^3-hybridized graphitic carbon (denoted by D band) and the vibration indexed to sp^2-hybridized graphitic carbon (denoted by G band), respectively [31, 32]. A characteristic strong peak around 2706 cm^{-1} is observed for the second order D (G*)-band, signature nature of graphitic sp^2 materials, produced by a second order resonance process. The relative degree of crystallographic defects/disorder and graphitic structure of the substrate can be determined from the intensity ratios I_D/I_G and I_{G*}/I_G [31, 32]. The I_D/I_G ratio for graphene (C) (0.75) is found to be slightly greater than that of CuO_X/C (0.72) and $PdCuO_X/C$ (0.41), which implies a higher graphitic structure [33].

FTIR analysis was done to investigate the functional groups and metal-oxygen bonds in the NPs and the spectra of $PdCuO_X$, CuO_X, CuO_X/C, and $PdCuO_X/C$ as presented in Figure 6.1c. The peak observed at 3454 and 3338 cm^{-1} could be assigned to the stretching vibration of free O-H and hydrogen bonded O-H groups, respectively from $Cu(OH)_2$ [34-37]. Another peak at 1670 cm^{-1} is ascribed to the bending vibration of OH group [34-37]. On the other hand, the peaks at 825, 1365 and 1348 cm^{-1} can be attributed to Cu-OH vibration mode of $Cu(OH)_2$ [34-37]. The presence of Cu(II)–O bond peaks can be confirmed by observing peaks at 508, 1000 cm^{-1} while Cu(I)-O vibrations confirmed by its characteristic peak at 624 cm^{-1} [34, 35]. Additionally, the appearance of two peaks in CuO_X/C and $PdCuO_X/C$ at 2932 and 2858 cm^{-1} are ascribed to the C−H stretching mode, suggesting the presence of graphene support [38]. All the peaks assigned to CuO_X and graphene can be seen in the $PdCuO_X/C$ hybrid NPs, confirming its formation.

TGA was carried out in air atmosphere to determine metal loading over the graphene support. For both $PdCuO_X/C$ and CuO_X/C Figure 6.1d it can be seen the mass loss is observed around 300 ºC which can be ascribed to the CO_2 formation in the air atmosphere and reaches a steady stable state at 450-500 ºC. These results confirm the metal loading for both $PdCuO_X/C$ and CuO_X/C over graphene support is 20% and which matches well with the calculation taken during the synthesis.

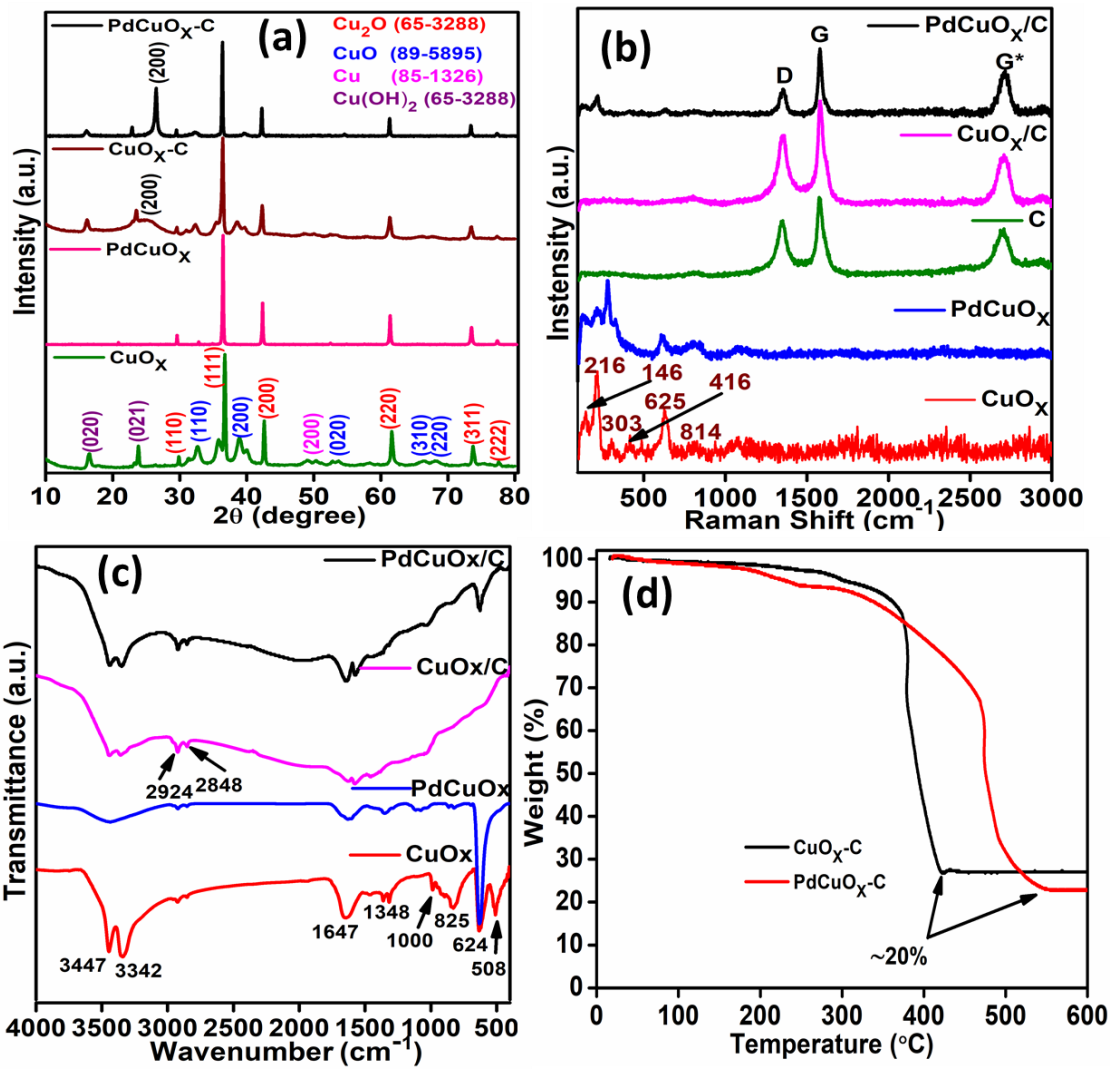

Figure 6.1: (a) PXRD of $PdCuO_X/C$, CuO_X/C, $PdCuO_X$, and CuO_X, (b) Raman spectra of $PdCuO_X/C$, CuO_X/C, graphene (C), $PdCuO_X$, and CuO_X, (c) FTIR spectra of $PdCuO_X$, CuO_X, CuO_X/C, and $PdCuO_X/C$, (d) TGA profile of $PdCuO_X/C$ and CuO_X/C in air atmosphere.

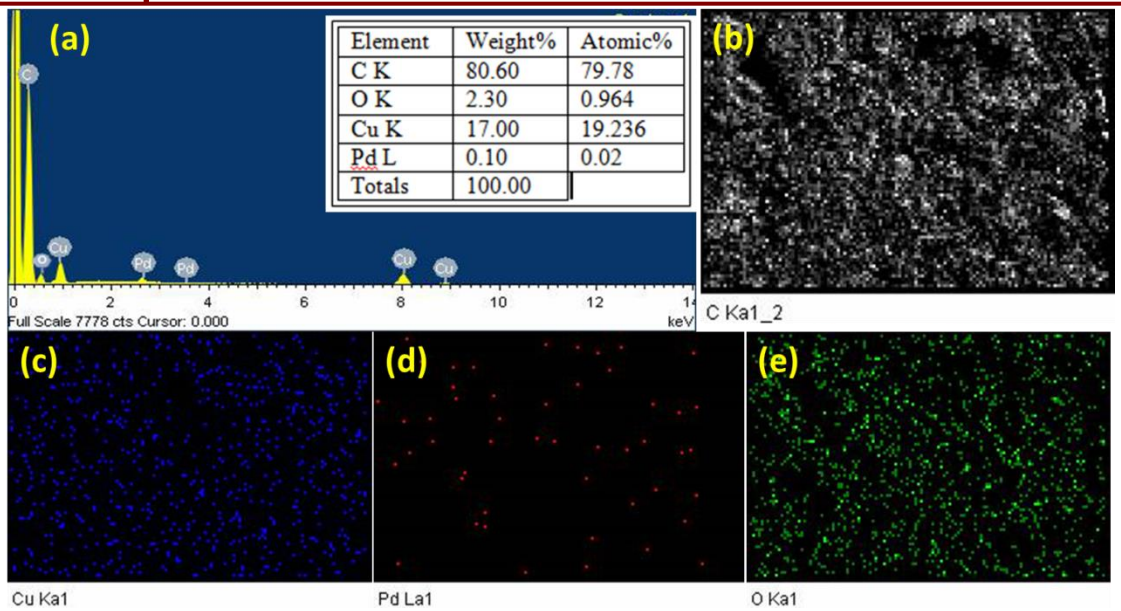

Figure 6.2: EDX analysis of $PdCuO_X/C$: (a) the EDX spectrum, and (b-e) elemental maps for individual C, Cu, Pd, and O, respectively.

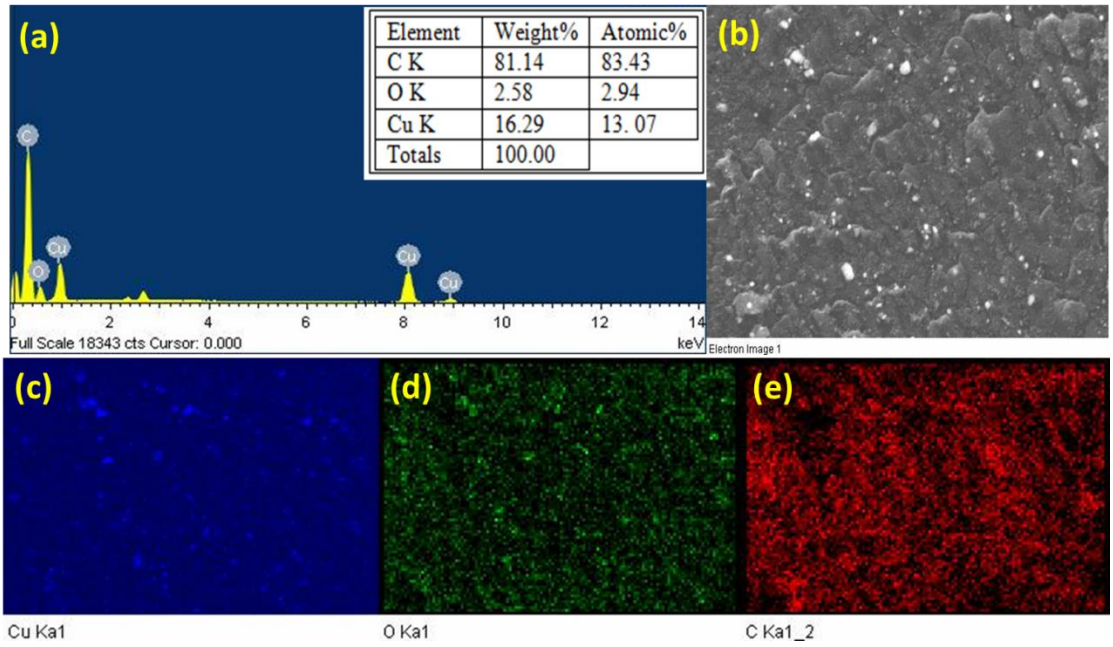

Figure 6.3: EDX analysis of CuO_X/C: (a) EDX spectrum, (b) the electron image and (c)-(e) elemental maps for individual Cu, O and C, respectively.

The atomic ratio of the elements on the graphene support was determined by EDX analysis. As revealed in Figure 6.2 the elemental maps of $PdCuO_X/C$, Pd Cu and O elements are homogeneously distributed on the graphene support. The atomic percentages of Pd and Cu are 0.02 and 19.236 which are in the ratio of 1:1000, confirming the

presence of a higher content of Cu than Pd. This ratio agrees well with the theoretical calculation taken during the synthesis. Similarly, for CuO_X/C the elemental composition spectra and atomic ratio for C, Cu and O presented in Figure 6.3 are in accordance with the theoretical calculation. Moreover, the respective elemental maps of CuO_X/C confirm that C, O, and Cu elements are present and distributed uniformly (Figure 6.3c-e). The total carbon to metal ratio in $PdCuO_X/C$ and CuO_X/C obtained from EDX analysis matches well with the TGA findings i.e., 80:20 ratio.

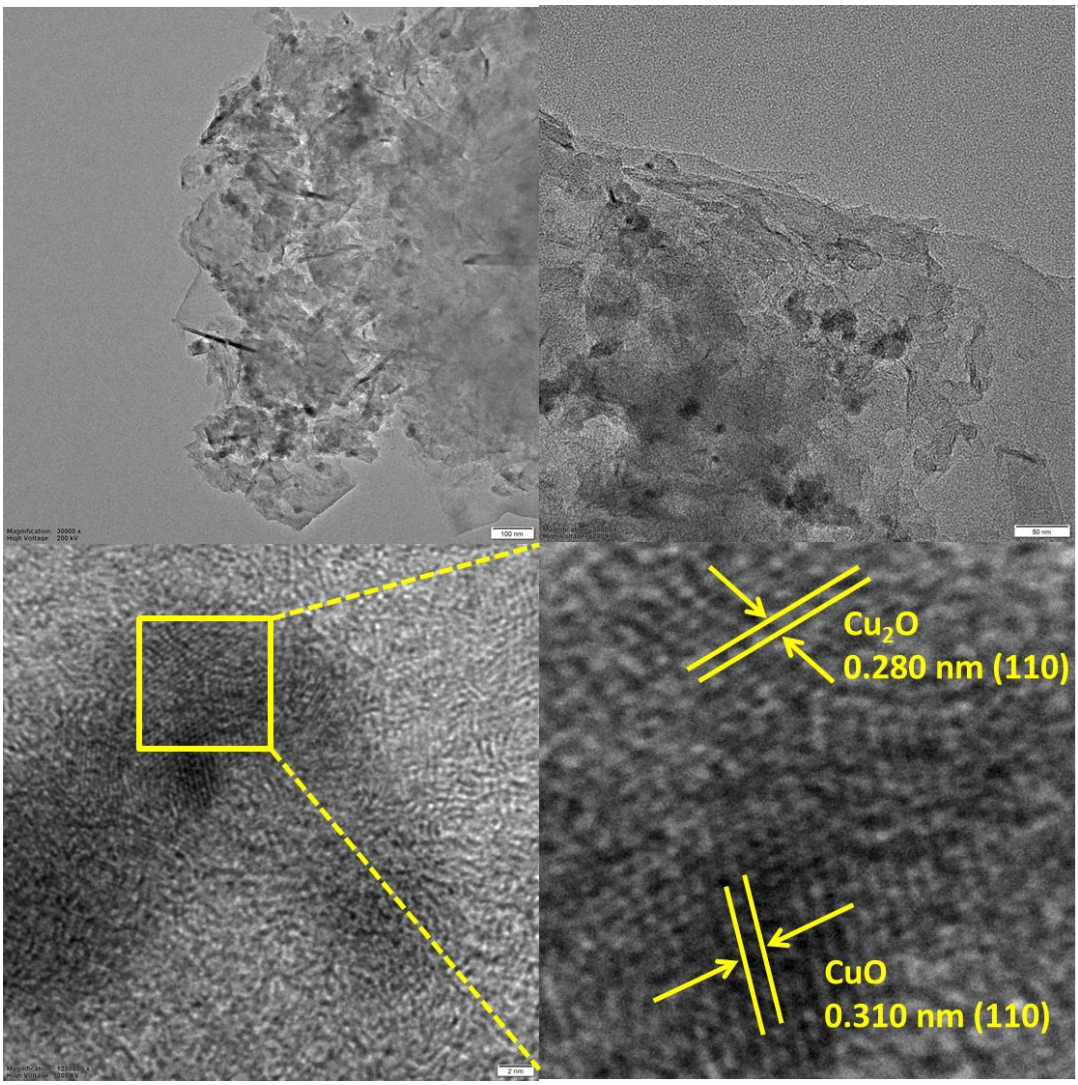

Figure 6.4: (a) High and (b) low-magnification TEM images of $PdCuO_X/C$, (c) high-resolution TEM (HRTEM) image of $PdCuO_X/C$ and (d) the magnified HRTEM image of the region marked by squares in (c).

TEM and HRTEM are analyses were carried out to characterize the morphology and microstructure of the as-synthesized NPs (Figure 6.4). It is easily discerned that $PdCuO_X$ is finely dispersed on the graphene surface and no obvious agglomeration of NPs are observed (Figure 6.4a, b). The dispersions of $PdCuO_X$ on the graphene could assist in expanding the space between graphene supports, which in turn promotes the diffusion of O_2 to reach the $PdCuO_X$ surface and thus improves ORR [34,35]. The TEM images reveal that graphene sheets are folded and have wrinkled morphology, which can be attributed to the 2D layer structure. The HRTEM image indicates that interplanar distances are 0.280 nm and 0.310 nm, which corresponds to the (110) facet of face-centered cubic (*fcc*) CuO and (110) monoclinic facet of CuO denoted by yellow lines. These results corroborated well with the p-XRD results of the $PdCuO_X/C$. Figure 6.4d represents the HRTEM image obtained from a magnified portion of Figure 6.4c. The distinct lattice fringes infer the good crystallinity of $PdCuO_X$ NPs over the graphene surface. The $PdCuO_X$ NPs strongly anchored on the graphene, which causes a strong interaction between them, increasing the facile charge transfer between $PdCuO_X$ and graphene [19, 20, 39, 40].

XPS was carried out to gain more information about the chemical bonds and oxidation state the as-synthesized $PdCuO_X/C$. Figure 6.5a displays the survey spectra of the corresponding elements. The identified peaks indicate the presence of Cu, Pd, O, and C; these results match well with the EDX spectra. The deconvoluted Pd 3d, Cu 2p, O 1s and C 1s spectra are presented in Figure 6.5b–e. Distinct peaks can be clearly seen in the Pd 3d XPS spectrum, the peaks at 336.0 eV and 341.4 eV mainly ascribed to Pd $3d_{5/2}$ and Pd $3d_{3/2}$, respectively (Figure 6.5b). The peaks in the Pd 3d region located at 336.0 eV and 341.4 eV were attributed to Pd^0 and the peaks at 337.9 eV and 343.4 eV were attributed to Pd^{2+} [39-41]. Likewise, Cu 2p spectrum (Figure 6.5c) depicts a doublet shape with the Cu $2p_{3/2}$ peak centered at 933 eV and the Cu $2p_{1/2}$ peak centered at 954 eV. After deconvolution of the Cu $2p_{3/2}$ peaks, the peaks located at 932.5 and 934.6 eV can be assigned to the Cu^0/Cu^+ and Cu^{2+}, respectively. Similarly, for Cu $2p_{1/2}$, the peaks at 952.4 and 954.3 eV related to the Cu^0/Cu^+ and Cu^{2+}, respectively [40, 42-45]. Moreover, the three satellite peaks located at 941.8, 944.2 and 962.5 eV are attributed to Cu $2p_{3/2}$ and Cu $2p_{1/2}$, respectively [42-45]. For the O 1s region presented in Figure 6.5d three peaks located at 530.8, 531.5 and 533 eV are assigned for O^{2-} of Cu-O bond, adsorbed oxygen

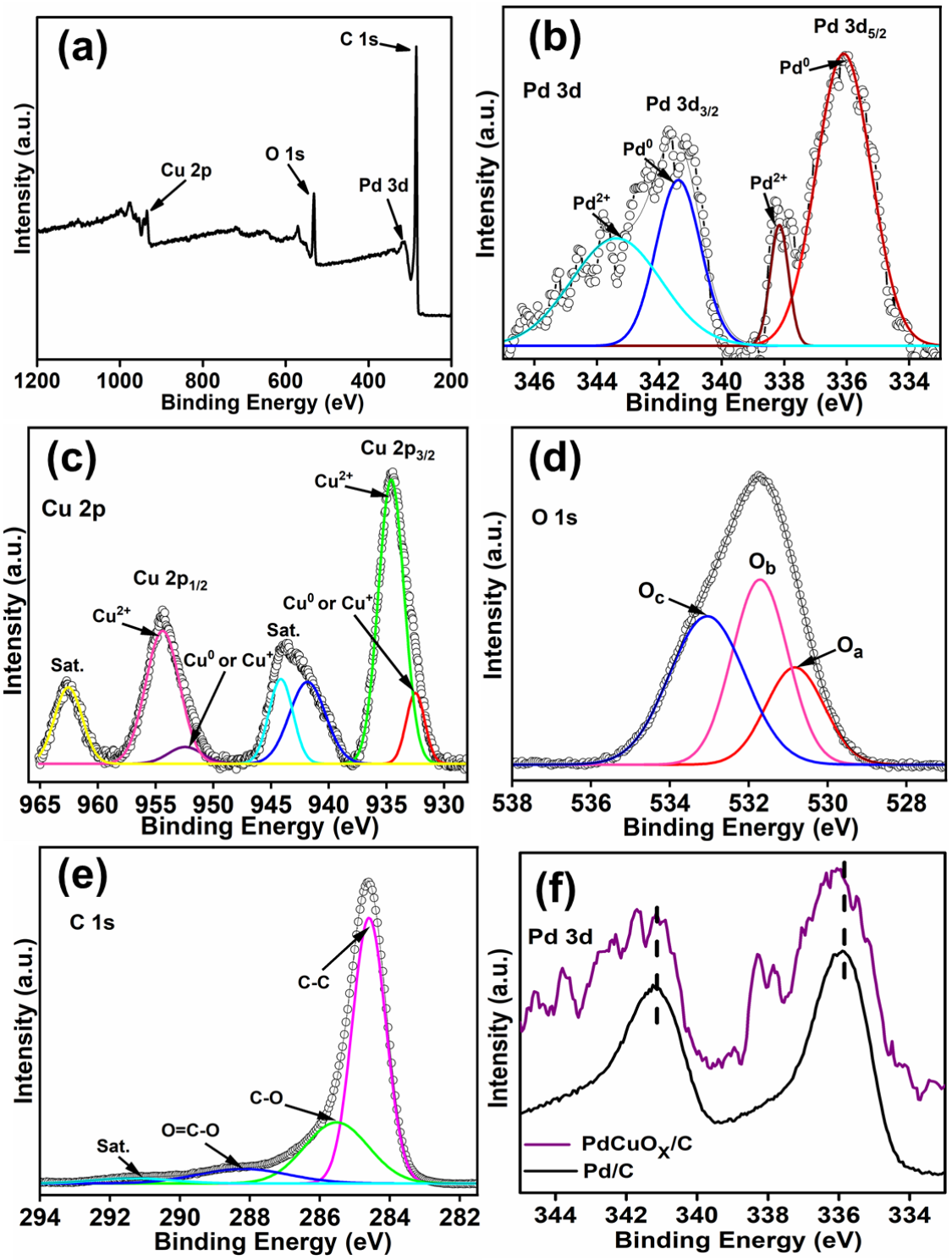

Figure 6.5: (a) XPS survey spectrum, high resolution XPS spectra of (b) Pd 3d, (c) Cu 2p, (d) O 1s, (e) C 1s and (f) correlation of binding energy change of Pd 3d of $PdCuO_X/C$ and Pd/C.

and physisorbed or chemisorbed H_2O molecules, respectively on the $PdCuO_X/C$ surface [42, 43, 46, 47]. Similarly, the C 1s spectrum showed three peaks centered at 284.6, 286.0 and 288.2 eV which are corresponded to C−C/C=C, C−O, and O=C−O, respectively (Figure 6.5e). And a satellite peak observed around 291 eV is due to π-π* transition [48]. The Pd 3d spectrum of $PdCuO_X/C$ and Pd/C are compared and a slight shift in the binding energy of Pd^0 of $PdCuO_X/C$ was observed than Pd/C (Figure 6.5f), which implicates the lowering of Pd *d*-band center. According to the *d*-band center theory, charge transfer to Pd results in a downward shift in the Pd *d*-band center, which reduces adsorbates interaction and improves ORR activity [1, 2, 40].

6.2.2. Electrocatalytic Activity towards ORR

CV and LSV analyses were done to evaluate the ORR activity of the prepared electrocatalysts. CV in both N_2 and O_2-enriched environments were assessed and presented in Figure 6.6a. It is easily discerned that in an O_2-enriched environment, an obvious and positive reduction peak is observed, which is superior to N_2-enriched, implying $PdCuO_X/C$ is catalytically active towards ORR. The LSV analyses were performed at a rotation rate of 400 to 3600 rpm and a scan rate of 10 mV s^{-1}. Figure 6.6b shows a steady rise in ORR current with increased rotation speed, suggesting that diffusion controls the ORR process [8, 40, 43]. The linear relationship of the K-L plot shown in Figure 6.6c validates the first-order reaction kinetics of ORR. Furthermore, the electrons transfer number (n) during the ORR process is determined using the K–L equation (discussed in Chapter 2). The n value of $PdCuO_X/C$ is 4 within the potential range of 0.50–0.75V *vs.* RHE, showing a direct $4e^-$ process and form OH^- without any intermediate depicted in Figure 6.6d.

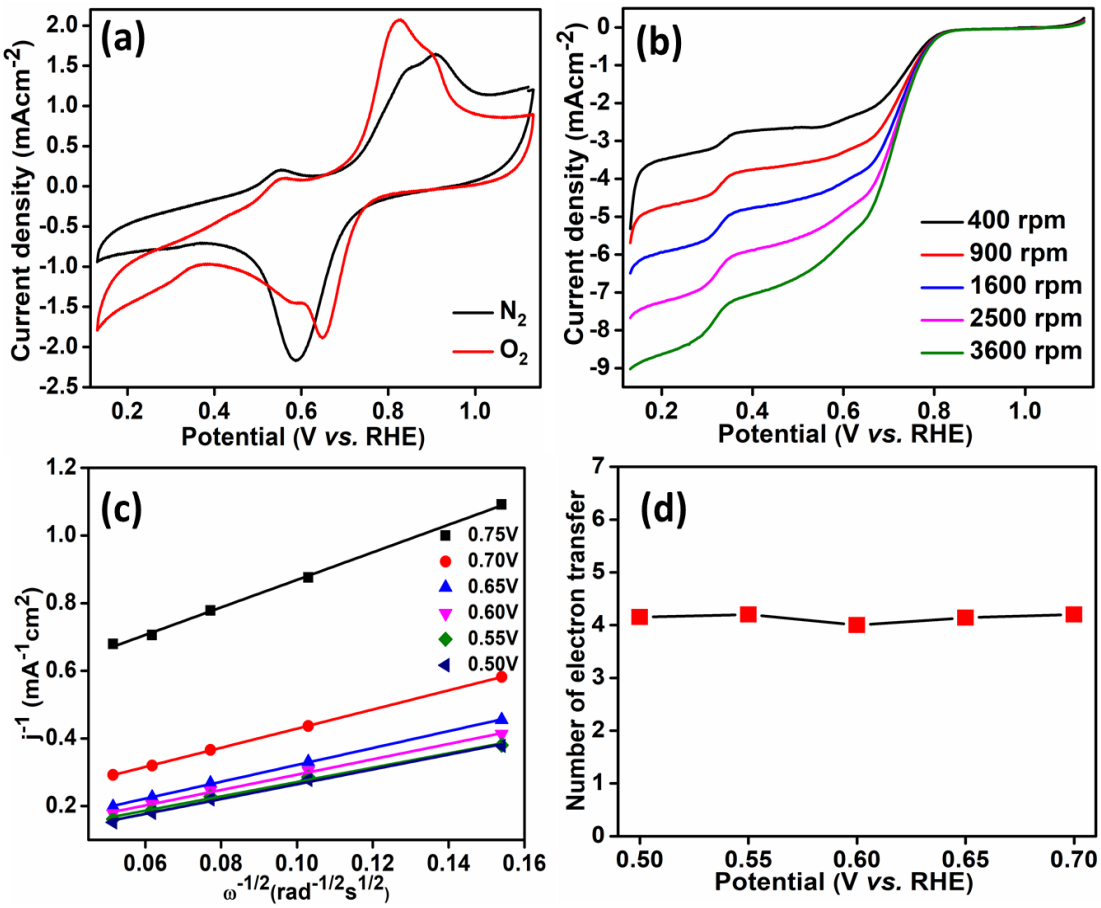

Figure 6.6: (a) CV plots of $PdCuO_X/C$ in N_2 and O_2-saturated 0.1 M KOH solution, (b) LSV plots at various rotation rate at 10 mVs^{-1} in O_2-saturated 0.1 M KOH of $PdCuO_X/C$, (c) corresponding K–L plots at various potentials and (d) plot of electron transfer number *vs.* potential of $PdCuO_X/C$.

The ORR activities of the $PdCuO_X$, CuO_X and CuO_X/C were systematically investigated in N_2- and O_2-saturated 0.1 M KOH electrolyte using CV and LSV analysis. The CV plots of the $PdCuO_X$, CuO_X and CuO_X/C in the potential window of 0.2-1.2 V (*vs.* RHE) at 50 mV s^{-1} is represented in Figure 6.7. A distinct reduction peak is observed in an O_2-saturated environment, suggesting that the electrocatalysts are active towards ORR. Similarly, the LSV curves are also plotted (Figure 6.8) at different rotations in O_2-saturated environment to get the kinetic information. From the LSV plots, the corresponding KL plots at mixed controlled regions are plotted and presented in Figure 6.9. The parallel and linear K–L plots are observed for all the electrocatalysts.

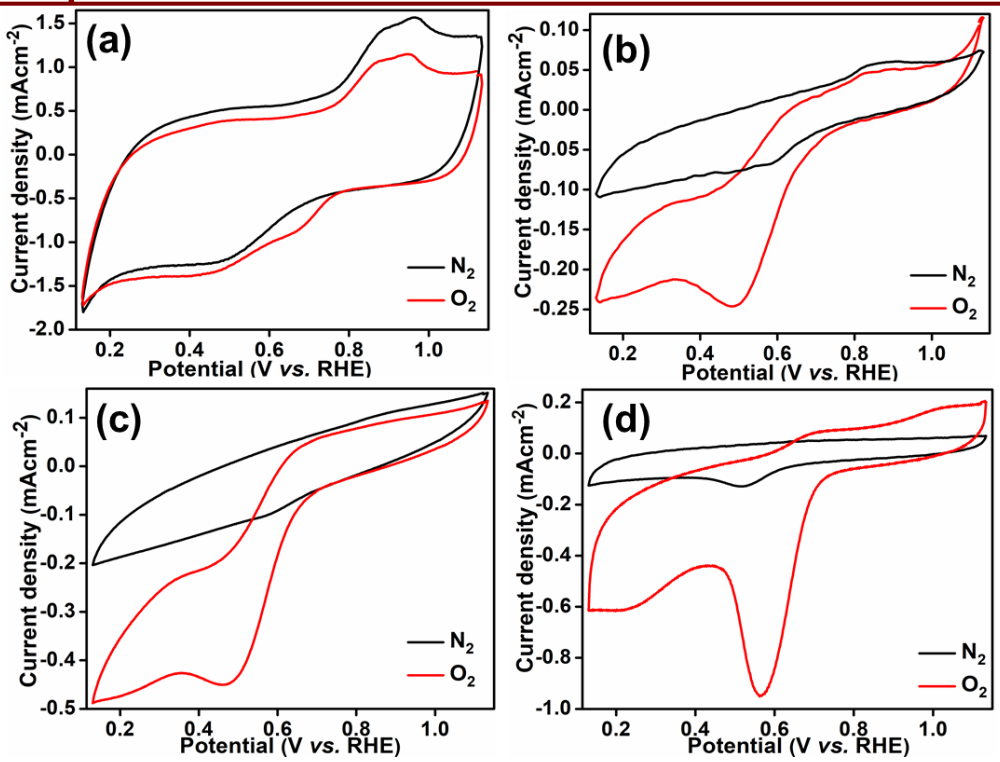

Figure 6.7: CV curves of (a) CuO_X/C, (b) $PdCuO_X$, (c) CuO_X and (d) C (graphene) in N_2 and O_2-saturated 0.1 M KOH.

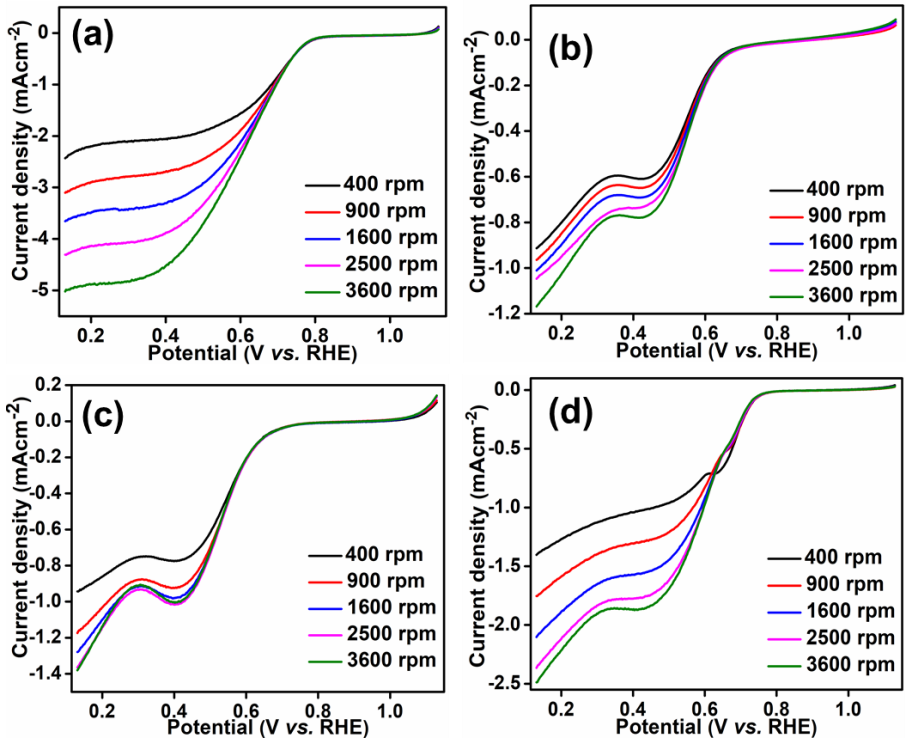

Figure 6.8: LSV curves of (a) CuO_X/C, (b) $PdCuO_X$, (c) CuO_X and (d) C at different rotations rate.

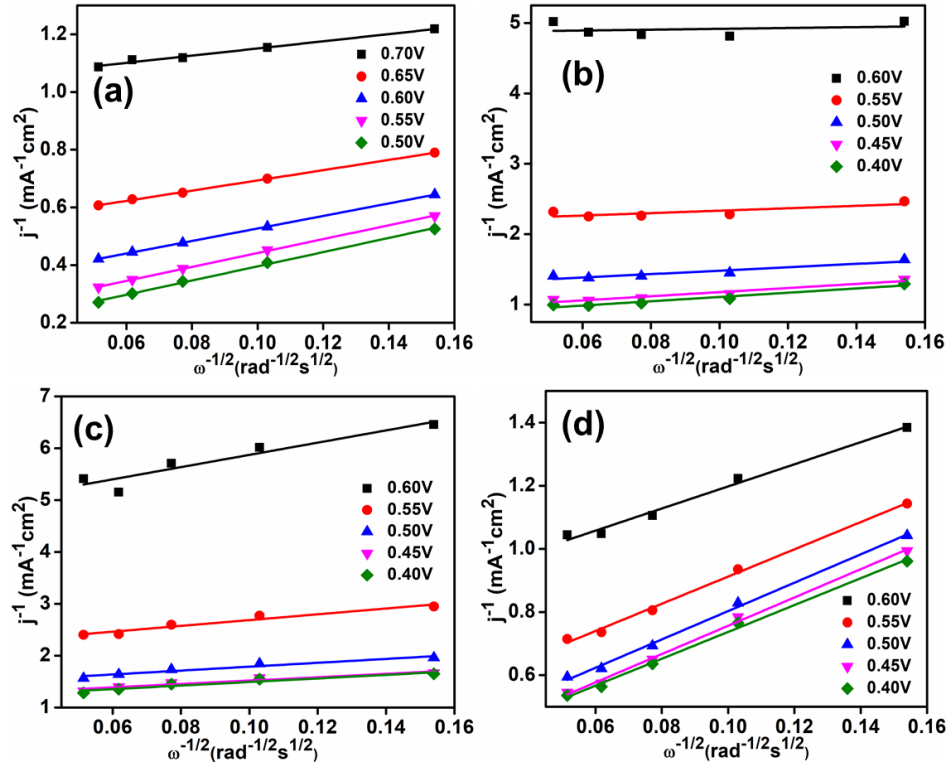

Figure 6.9: K–L plots at various potentials for (a) CuO_X/C, (b) $PdCuO_X$, (c) CuO_X and (d) C derived from LSV curves at 1600 rpm rotation speeds.

The LSV curves for all the electrocatalysts are compared in O_2-saturated electrolyte at 1600 rpm are represented in Figure 6.10a. It is observed the onset potential (E_{onset}) values of $PdCuO_X/C$, CuO_X/C, $PdCuO_X$ and CuO_X are 0.86, 0.82, 0.68, and 0.67 V, respectively. Notably, the limiting current density (j_m) of $PdCuO_X/C$ is also higher than the other electrocatalysts. Similarly, $PdCuO_X/C$ displays 9mV, 17mV, and 18mV positive half wave potential ($E_{1/2}$) than CuO_X/C, $PdCuO_X$ and CuO_X, respectively in Figure 6.10b. The superior ORR performance of $PdCuO_X/C$ is attributed to the efficient electronic conduction and interaction between both the $PdCuO_X$ and C support. The electrochemical parameters of all the electrocatalysts were tabulated in Table 6.1. It is widely known that the MA of the catalyst is closely associated with the cost of FCs in real-world applications [40, 43]. The polarization curve is normalized to the mass of the catalyst on the electrode surface to evaluate the MA of the catalyst.

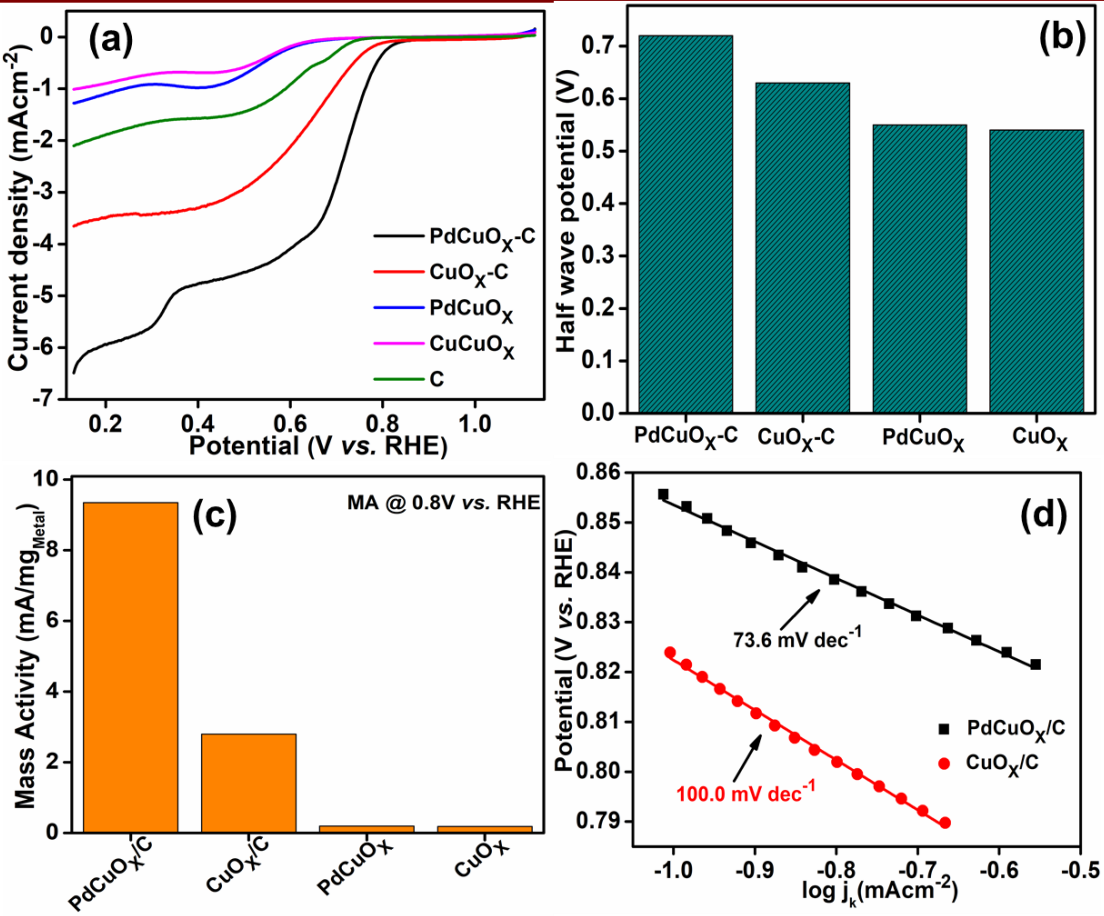

Figure 6.10: (a) Comparison of LSV plots of $PdCuO_X/C$, CuO_X/C, $PdCuO_X$, CuO_X, and C at 1600 rpm in O_2-saturated 0.1M KOH solution, (b) comparison of half wave potential ($E_{1/2}$) of $PdCuO_X/C$, CuO_X/C, $PdCuO_X$, and CuO_X, (c) mass-specific activity of the electrocatalysts at 0.80 V and (d) Tafel slope of $PdCuO_X/C$ and CuO_X/C.

The mass specific activity (MA) of all the electrocatalysts are compared at the same potential (Figure 6.10c). The MA of $PdCuO_X/C$ is 3.2, 48.2, and 48.4 times higher than the CuO_X/C, $PdCuO_X$ and CuO_X, respectively. It can say that with the same amount of mass loading on the electrode, we observed a higher MA for $PdCuO_X/C$, which signifies the high utilization of metal loading towards ORR. The ORR kinetics of the electrocatalysts were evaluated using the Tafel plots, which were obtained by plotting the log of the kinetic current density (log J_k) obtained from the LSV curve *vs.* potential (V). The Tafel slope of $PdCuO_X/C$ (73.6 $mVdec^{-1}$), as depicted in Figure 6.10d, is the lowest compared to CuO_X/C (100 $mVdec^{-1}$) and the smaller Tafel slope of associated with the faster ORR kinetics.

Table 6.1: Summary of the electrochemical parameters for ORR of the as-synthesized electrocatalysts

Electrocatalysts	**E_{onset} (V *vs.* RHE)**	**$E_{1/2}$ (V *vs.* RHE)**	**Number of electron transfer (n)**	**ECSA (m^2g^{-1})**
$PdCuO_X/C$	0.86	0.72	4.1	79.0
CuO_X/C	0.82	0.63	3.6	21.6
$PdCuO_X$	0.68	0.55	3.2	3.0
CuO_X	0.67	0.54	2.4	5.1

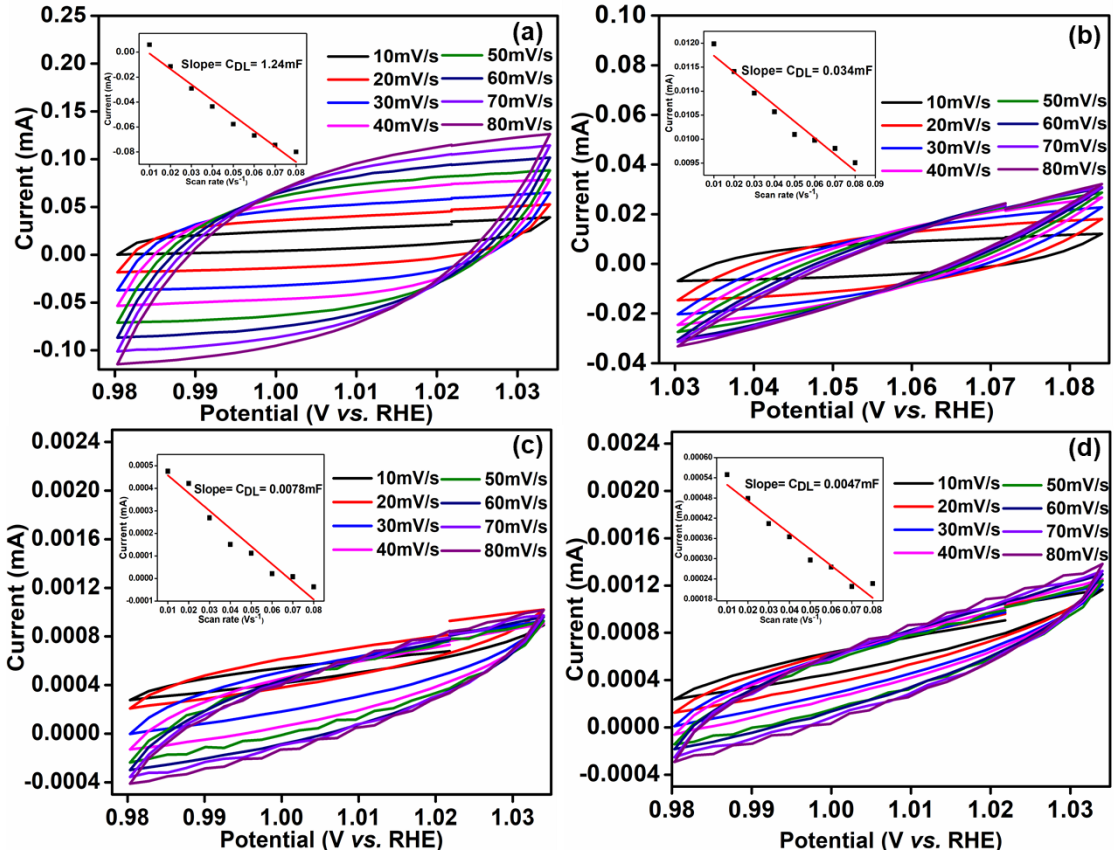

Figure 6.11: CV measurements for determining ECSA in 0.1 M KOH (a-d) represent CV plots of $PdCuO_X/C$, CuO_X/C, CuO_X and $PdCuO_X$, respectively, at different scan rates in the non-faradaic region (insets show the corresponding slope (C_{DL}) obtained from respective CV data).

The ECSA reflects the surface area associated with the electronic interaction between the catalyst's and the electrolyte's surfaces during the non-faradaic reaction. As shown in Figure 6.11, the CV in the non-faradaic region was acquired at different scan rates i.e., 10, 20, 30, 40, 50, and 60 mV/s. The ECSA of the catalysts were calculated by the double-layer capacitance (C_{dl}) using CV analysis in the non-Faradaic range. The value of C_{dl} is obtained by plotting half of the anodic current−cathodic current (ja−jc/2) against the scan rate [43, 49]. The formula for calculating ECSA was mentioned in Chapter 2. The ECSAs of $PdCuO_X/C$, CuO_X/C, CuO_X and $PdCuO_X$ is 79.0 21.6, 5.1 and 3.0 m^2g^{-1}**,** respectively. The ECSA of $PdCuO_X/C$ is 3.6, 15.4 and 26.3 times larger than that of CuO_X/C, CuO_X and $PdCuO_X$, respectively. In comparison with the other catalysts, the larger value of $PdCuO_X/C$ suggests a number of active sites present in the material, which is advantageous for improving the active surface area. The higher ECSA values on $PdCuO_X/C$ indicate that the $PdCuO_X$ NPs supported by graphene are well exposed to the electrolyte, resulting in the $PdCuO_X$ NPs being evenly distributed on the surface of the graphene.

Long-term stability and durability are crucial criteria for ORR catalysts to be used in practical applications. The durability of the catalyst was evaluated by continuous CV measurement for 10000 redox cycles within the range of 0.50- 0.90 V (*vs.* RHE) in an O_2-saturated 0.1 M KOH solution. The LSV polarization curve of both before and after 10000 cycles was compared, as shown in Figure 6.12a. There is almost no change in E_{onset} and $E_{1/2}$ of $PdCuO_X/C$, whereas for CuO_X/C, the $E_{1/2}$ is declined by 9 mV (Figure 6.12b). These results suggest that $PdCuO_X/C$ infers impressive stability and durability behaviour. Moreover, after the 6 h of stability test (Figure 6.12c), the decay of the current density of $PdCuO_X/C$ is only 6.1% of the initial current, whereas, for Pt/C and CuO_X/C, the current decay is 27.5% and 17.5%, respectively, indicating that $PdCuO_X/C$ has commendable long-term durability.

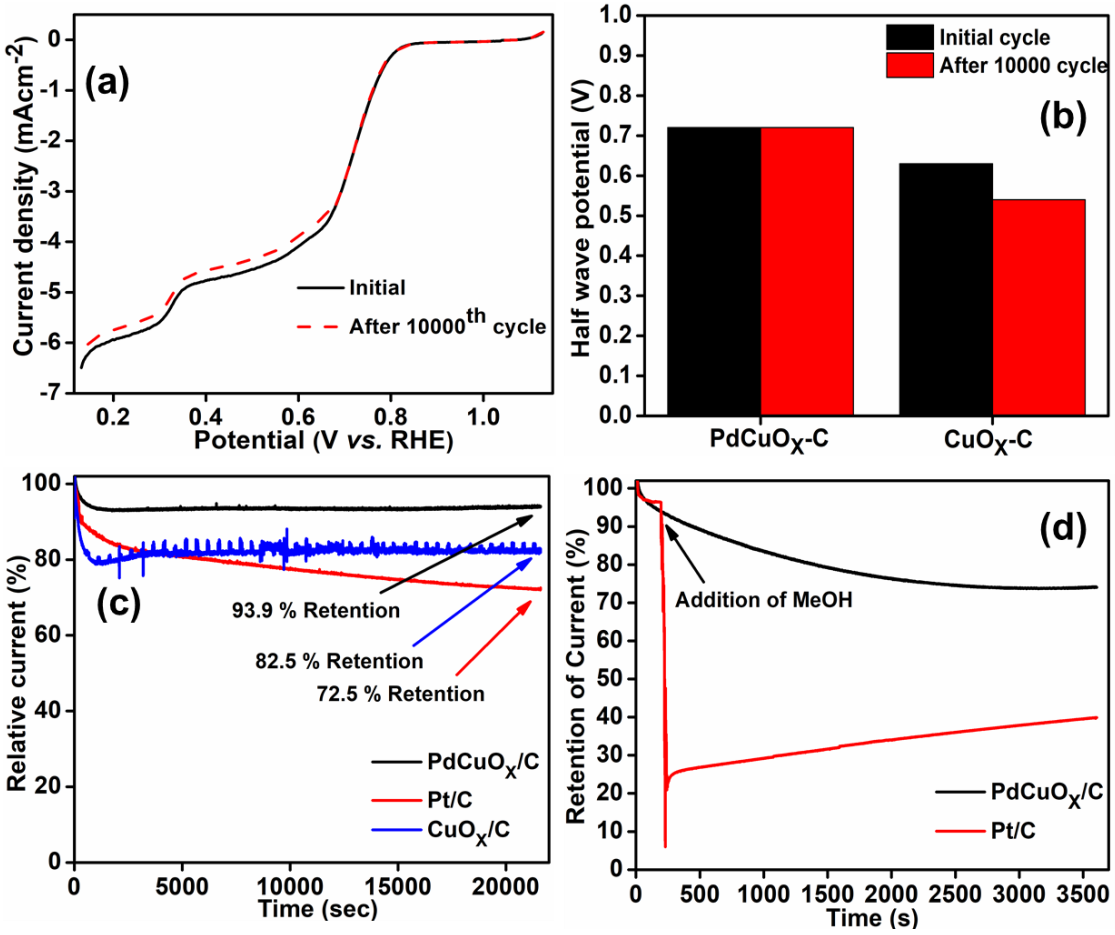

Figure 6.12: (a) ORR polarization LSV plots of $PdCuO_X/C$ before and after 10000 cycles at 1600 rpm, (b) comparison of $E_{1/2}$ of $PdCuO_X/C$ and CuO_X/C before and after 10000 cycles, (c) chronoamperometry (CA) plots of $PdCuO_X/C$, CuO_X/C and Pt/C measured in an O_2-saturated 0.1 M KOH at a rotation of 1600 rpm and (d) CA plots of a CH_3OH tolerance test of $PdCuO_X/C$ and commercial Pt/C for 3600 s.

The methanol crossover from the anode to the cathode in direct methanol fuel cells (DMFCs), in particular, causes a drop in utilization efficiency and in the output power of FCs and a rise in the oxygen demand. To solve this problem, it is urgent for researchers to search for very efficient, long-term, cost-effective metal catalysts that are methanol-tolerant. So, for the MeOH crossover study, a calculated amount of MeOH was injected into the alkaline electrolyte with O_2-sparging. The CA peak of Pt/C showed rapid current drops upon injecting MeOH at 200s, but it stayed unaltered for $PdCuO_X/C$ in Figure 6.12d, demonstrating high MeOH tolerance.

Table 6.2: Comparison of the ORR parameters of CuO_X-based electrocatalysts in 0.1 M KOH

Electrocatalyst	**E_{onset} V (*vs.* RHE)**	**$E_{1/2}$ V (*vs.* RHE)**	**Tafel (mV dec^{-1})**	**References**
$PdCuO_X/C$	0.86	0.72	73.6	This work
CuO–NiO/rGO composite	0.80	-	72	44
CuO/G	0.80	-	141	45
$Ag/Cu_xO/C$	0.86	0.80	46	46
Cu_2O/C	0.81	0.72	-	47
Cu(15%)-MFC60	0.86	0.76	82	48
Co_3O_4–$CuO/Cu_2O/C$	0.867	0.721	83.6	49
Cu-P-C-800	0.86	0.83	71	50
Cu/Cu_2O-NC	0.85	0.80	106	51

Table 6.2 compares the ORR electrokinetic parameters including E_{onset}, $E_{1/2}$ and Tafel slope of several Cu-based catalysts reported in 0.1M KOH electrolyte. A comparatively greater or similar E_{onset} and $E_{1/2}$ were observed for $PdCuO_X/C$ than the other Cu-carbon based electrocatalysts [49-56]. The Tafel slope of $PdCuO_X/C$ is smaller than the CuO/G [50], Cu(15%)-MFC60 [53], Co_3O_4–$CuO/Cu_2O/C$ [54], and Cu/Cu_2O-NC [56] suggesting faster kinetics. From these results, we can say that $PdCuO_X/C$ exhibits more remarkable ORR performance than its counterpart. The substantially superior performance of the $PdCuO_X/C$ catalyst can be attributed to (1) the development of ultrathin graphene, which is conductive and facilitates electron transportation, (2) A large number of catalytic active sites evident from ECSA is provided by the existence of metal or metal oxide in a well-dispersed form improves the transfer of electron during electrochemical reactions, (3) A high electron density at the interface between graphene and metal/metal oxide enhances the performance, (4) The charge transfer between the Pd

and CuO_X and the strong synergistic interaction substantially enhanced the catalytic activity. Moreover, in correlation to the previous chapters in the present chapter, we aim to decrease the Pd loading and synthesize $PdCuO_X/C$. With this small amount of Pd loading, the reported electrocatalyst exhibits commendable performance in terms of stability and durability. The admirable electrocatalytic activity of the resultant hybrid NPs can be directly attributed to its larger ECSA and synergistic effects between Pd and CuO_X. In this regard, $PdCuO_X/C$ can be a promising electrode material for oxygen reduction electrocatalysis. It may be a more affordable and economical electrocatalyst for FCs than the ones currently available.

6.3. Conclusions

A facile solvothermal method assisted by carbonization was adopted to synthesize $PdCuO_X/C$ and CuO_X/C. This study demonstrated that introducing Pd in the CuO_X/C played a crucial role in the ORR performance of $PdCuO_X/C$ hybrid NPs. As shown by the results of PXRD, TEM-HRTEM, XPS and EDS mapping, $PdCuO_X$ NPs are successfully and uniformly dispersed on the surface of graphene nanosheets. The as-prepared $PdCuO_X/C$ demonstrated enhanced ORR performance with an E_{onset} of 0.86 V and $E_{1/2}$ of 0.72 V *vs.* RHE, surpassing that of its counterparts. Furthermore, it exhibits excellent methanol tolerance, remarkable durability, and rapid ORR kinetics. Even after six long hours, the $PdCuO_X/C$ can retain 93.9% of its original performance, exhibiting incredible stability. The ultralow load of Pd lowers costs and forms a highly efficient electrocatalyst thanks to the synergistic interactions between CuO_X and Pd. These findings imply that the $PdCuO_X/C$ opens new avenues for low loading of noble catalysts in the domains of energy conversion devices.

References

[1] Wang, T., Chutia, A., Brett, D.J., Shearing, P.R., He, G., Chai, G. and Parkin, I.P. Palladium alloys used as electrocatalysts for the oxygen reduction reaction. *Energy & Environmental Science*, 14(5):2639-2669, 2021.

[2] Erikson, H., Sarapuu, A., Solla-Gullón, J. and Tammeveski, K. Recent progress in oxygen reduction electrocatalysis on Pd-based catalysts. *Journal of Electroanalytical Chemistry*, 780:327-336, 2016.

[3] Zhou, M., Guo, J. and Fang, J. Nanoscale design of Pd-based electrocatalysts for oxygen reduction reaction enhancement in alkaline media. *Small Structures*, 3(2):2100188, 2022.

[4] Wang, Y., Li, J. and Wei, Z. Transition-metal-oxide-based catalysts for the oxygen reduction reaction. *Journal of Materials Chemistry A*, 6(18):8194-8209, 2018.

[5] Goswami, C., Hazarika, K.K. and Bharali, P. Transition metal oxide nanocatalysts for oxygen reduction reaction. *Materials Science for Energy Technologies*, 1(2):117-128, 2018.

[6] Xiong, W., Yin, H., Wu, T. and Li, H. Challenges and opportunities of transition metal oxides as electrocatalysts. *Chemistry–A European Journal*, 29(5):202202872, 2023.

[7] Saianand, G., Gopalan, A.I., Lee, J.C., Sathish, C.I., Gopalakrishnan, K., Unni, G.E., Shanbhag, D., Dasireddy, V.D., Yi, J., Xi, S. and Al-Muhtaseb, A.A.H. Mixed copper/copper-oxide anchored mesoporous fullerene nanohybrids as superior electrocatalysts toward oxygen reduction reaction. *Small*, 16(12):1903937, 2020.

[8] Zhou, R., Zheng, Y., Hulicova-Jurcakova, D. and Qiao, S.Z. Enhanced electrochemical catalytic activity by copper oxide grown on nitrogen-doped reduced graphene oxide. *Journal of Materials Chemistry A*, 1(42):13179-13185, 2013.

[9] Xu, G., Huang, J., Li, X., Chen, Q., Xie, Y., Liu, Z., Kajiyoshi, K., Wu, L., Cao, L. and Feng, L. Heterostructured Cu/CuO nanoparticles embedded within N-doped carbon nanosheets for efficient oxygen reduction reaction. *Catalysts*, 13(2):255, 2023.

[10] Yan, X.Y., Tong, X.L., Zhang, Y.F., Han, X.D., Wang, Y.Y., Jin, G.Q., Qin, Y. and Guo, X.Y. Cuprous oxide nanoparticles dispersed on reduced graphene oxide

as an efficient electrocatalyst for oxygen reduction reaction. *Chemical Communications*, 48(13):1892-1894, 2012.

[11] Olabi, A.G., Abdelkareem, M.A., Wilberforce, T. and Sayed, E.T. Application of graphene in energy storage device–A review. *Renewable and Sustainable Energy Reviews*, 135:110026, 2021.

[12] Khater, D.Z., Amin, R.S., Mahmoud, M. and El-Khatib, K.M. Evaluation of mixed transition metal (Co, Mn, and Cu) oxide electrocatalysts anchored on different carbon supports for robust oxygen reduction reaction in neutral media. *RSC Advances*, 12(4):2207-2218, 2022.

[13] Chandrasekaran, S., Ma, D., Ge, Y., Deng, L., Bowen, C., Roscow, J., Zhang, Y., Lin, Z., Misra, R.D.K., Li, J. and Zhang, P. Electronic structure engineering on two-dimensional (2D) electrocatalytic materials for oxygen reduction, oxygen evolution, and hydrogen evolution reactions. *Nano Energy*, 77:105080, 2020.

[14] Zhang, W., Chang, J. and Yang, Y. Strong precious metal–metal oxide interaction for oxygen reduction reaction: A strategy for efficient catalyst design. *SusMat*, 3(1):2-20, 2023.

[15] Zhang, N. and Jiang, R. Interfacial engineering of metal/metal oxide heterojunctions toward oxygen reduction and evolution reactions. *ChemPlusChem*, 86(12):1586-1601, 2021.

[16] Hu, Q., Liu, X., Tang, C., Fan, L., Chai, X., Zhang, Q., Liu, J. and He, C. High efficiency oxygen evolution reaction enabled by 3D network composed of nitrogen-doped graphitic carbon-coated metal/metal oxide heterojunctions. *Electrochimica Acta*, 265:620-628, 2018.

[17] Choi, C.H., Park, S.H. and Woo, S.I. Oxygen reduction activity of Pd–Mn_3O_4 nanoparticles and performance enhancement by voltammetrically accelerated degradation. *Physical Chemistry Chemical Physics*, 14(19):6842-6848, 2012.

[18] Dhali, S., Pandey, S., Dandapat, A., Sahoo, T., Sahu, P.S., Saha, B. and Sahoo, N.G. Pd-Fe_2O_3 decorated nitrogen-doped reduced graphene oxide/CNT nanohybrids electrocatalyst for proton exchange membrane fuel cell. *Diamond and Related Materials*, 126:109115, 2022.

[19] Chen, H., Bao, L., Ou, C., Wang, H., Liao, Y., Li, R. and Liu, H., Highly dispersed and small-size Pd–Cu nanoparticles supported on N-doped graphene for oxygen reduction reaction catalysts. *Energy & Fuels*, 36(14):7699-7709, 2022.

[20] Zheng, Y., Zhao, S., Liu, S., Yin, H., Chen, Y.Y., Bao, J., Han, M. and Dai, Z. Component-controlled synthesis and assembly of Cu–Pd nanocrystals on graphene for oxygen reduction reaction. *ACS Applied Materials & Interfaces*, *7*(9):5347-5357, 2015.

[21] Zhu, J., Jiang, E., Wang, X., Pan, Z., Xu, X., Ma, S., Shen, P.K., Pan, L., Eguchi, M., Nanjundan, A.K. and Shapter, J. Gram-Scale production of Cu_3P-Cu_2O janus nanoparticles into nitrogen and phosphorous doped porous carbon framework as bifunctional electrocatalysts for overall water splitting. *Chemical Engineering Journal*, 427:130946, 2022.

[22] Qiu, X.Y., Liu, S.J. and Xu, D.Z. Yolk-shell structured Cu_2O as a high-performance cathode catalyst for the rechargeable Li-O_2 batteries. *Journal of Materials Science*, 53:1318-1325, 2018.

[23] Sahu, K., Singh, J. and Mohapatra, S. Photocatalytic and catalytic removal of toxic pollutants from water using CuO nanosheets. *Journal of Materials Science: Materials in Electronics*, 30:6088-6099, 2019.

[24] Li, X., Che, Y., Lv, Y., Liu, F., Wang, Y., Zhao, C. and Liu, C. Synthesis and characterization of CuZnO@GO nanocomposites and their enhanced antibacterial activity with visible light. *Journal of Sol-Gel Science and Technology*, 89:672-684, 2019.

[25] Zhou, X., Zhou, X., Liu, L., Chen, H., Hu, X., Qian, J., Huang, D., Zhang, B. and Tang, J. Self-supported Cu_3P nanowire electrode as an efficient electrocatalyst for the oxygen evolution reaction. *RSC Advances*, 11(54):34137-34143, 2021.

[26] Guo, J., Wang, X., Guo, Z., Guo, B., Wang, Z., Shang, Z., Ma, J. and Wu, M. Cu-based active sites supported on nitrogen-rich polymer derived porous carbon fibers as an oxygen reduction electrocatalyst for zinc-air batteries. *Carbon*, 228:119294, 2024.

[27] Xu, J.F., Ji, W., Shen, Z.X., Li, W.S., Tang, S.H., Ye, X.R., Jia, D.Z. and Xin, X.Q. Raman spectra of CuO nanocrystals. *Journal of Raman spectroscopy*, 30(5):413-415, 1999.

[28] Bruno, E., Haris, M., Mohan, A. and Senthilkumar, M. Temperature effect on CuO nanoparticles via facile hydrothermal approach to effective utilization of UV–visible region for photocatalytic activity. *Applied Physics A*, 127(12):925, 2021.

[29] Chen, L., Chen, C.C., Liang, K.C., Chang, S.H., Tseng, Z.L., Yeh, S.C., Chen,

C.T., Wu, W.T. and Wu, C.G., Nano-structured CuO-Cu_2O complex thin film for application in $CH_3NH_3PbI_3$ perovskite solar cells. *Nanoscale Research Letters*, 11(402):1-7, 2016.

[30] Pagare, P.K. and Torane, A.P. Band gap varied cuprous oxide (Cu_2O) thin films as a tool for glucose sensing. *Microchimica Acta*, 183:2983-2989, 2016.

[31] Ma, B., Rodriguez, R.D., Ruban, A., Pavlov, S. and Sheremet, E. The correlation between electrical conductivity and second-order Raman modes of laser-reduced graphene oxide. *Physical Chemistry Chemical Physics*, 21(19):10125-10134, 2019.

[32] Behnoudnia, F. and Dehghani, H. Copper (II) oxalate nanospheres and its usage in preparation of $Cu(OH)_2$, Cu_2O and CuO nanostructures: Synthesis and growth mechanism. *Polyhedron*, 56:102-108, 2013.

[33] Balık, M., Bulut, V. and Erdogan, I.Y. Optical, structural and phase transition properties of Cu_2O, CuO and Cu_2O/CuO: Their photoelectrochemical sensor applications. *International Journal of Hydrogen Energy*, 44(34):18744-18755, 2019.

[34] Akhavan, O., Ghaderi, E., Hashemi, E. and Rahighi, R. Ultra-sensitive detection of leukemia by graphene. *Nanoscale*, 6(24):14810-14819, 2014.

[35] Liu, M., Gan, L., Xiong, W., Xu, Z., Zhu, D. and Chen, L. Development of MnO_2/porous carbon microspheres with a partially graphitic structure for high performance supercapacitor electrodes. *Journal of Materials Chemistry A*, 2(8):2555-2562, 2014.

[36] Pramanik, A., Maiti, S. and Mahanty, S. Reduced graphene oxide anchored $Cu(OH)_2$ as a high performance electrochemical supercapacitor. *Dalton Transactions*, 44(33): 14604-14612, 2015.

[37] Devamani, R.H.P. and Alagar, M.J.N.B.E. Synthesis and characterisation of copper II hydroxide nano particles. *Nano Biomedicine and Engineering*, 5(3):116-120, 2013.

[38] Zhou, H., Han, G., Xiao, Y., Chang, Y. and Zhai, H.J. Facile preparation of polypyrrole/graphene oxide nanocomposites with large areal capacitance using electrochemical codeposition for supercapacitors. *Journal of Power Sources*, 263:259-267, 2014.

[39] Wu, X., Feng, B., Li, W., Niu, Y., Yu, Y., Lu, S., Zhong, C., Liu, P., Tian, Z., Chen, L. and Hu, W. Metal-support interaction boosted electrocatalysis of

ultrasmall iridium nanoparticles supported on nitrogen doped graphene for highly efficient water electrolysis in acidic and alkaline media. *Nano Energy*, 62:117-126, 2019.

[40] Chetry, R., Chutia, B., Patowary, S., Borah, B.J., Sudarsanam, P. and Bharali, P. Electronic modulation of Pd/C by simultaneous doping of Cu and Co tendering a highly durable and methanol-tolerant oxygen reduction electrocatalyst. *Energy & Fuels*, 37(13):9557-9567, 2023.

[41] Song, J., Xiao, Z., Jiang, Y., Abdelhafiz, A.A., Chang, I. and Zeng, J. Surfactant-free room temperature synthesis of Pd_xPt_y/C assisted by ultra-sonication as highly active and stable catalysts for formic acid oxidation. *International Journal of Hydrogen Energy*, 44(23):11655-11663, 2019.

[42] Adhikary, R., Sarkar, D., Mukherjee, M. and Datta, J. Remarkable performance of the unique Pd–Fe_2O_3 catalyst towards EOR and ORR: Non-Pt and non-carbon electrode materials for low-temperature fuel cells. *Journal of Materials Chemistry A*, 9(5):3052-3065, 2021.

[43] Goswami, C., Yamada, Y., Matus, E.V., Ismagilov, I.Z., Kerzhentsev, M. and Bharali, P. Elucidating the role of oxide–oxide/carbon interfaces of CuO_x–CeO_2/C in boosting electrocatalytic performance. *Langmuir*, 36(49):15141-15152, 2020.

[44] Singh, S.J., Sellaiyan, S. and Chinnamuthu, P. Synthesis and characterization of CuO/gC_3N_4 nanocomposite for efficient photocatalytic activities under natural sunlight. *Physica B: Condensed Matter*, 650:414543, 2023.

[45] Yu, B., Diniz, J., Lofgren, K., Liu, Q., Mercado, R., Nichols, F., Oliver, S.R. and Chen, S. Copper/carbon nanocomposites for electrocatalytic reduction of oxygen to hydrogen peroxide. *ACS Sustainable Chemistry & Engineering*, 10(47):15501-15507, 2022.

[46] Lv, W., Li, L., Meng, Q. and Zhang, X. Molybdenum-doped CuO nanosheets on Ni foams with extraordinary specific capacitance for advanced hybrid supercapacitors. *Journal of Materials Science*, 55(6):2492-2502, 2020.

[47] Singh, S.J., Sellaiyan, S. and Chinnamuthu, P. Synthesis and characterization of CuO/gC_3N_4 nanocomposite for efficient photocatalytic activities under natural sunlight. *Physica B: Condensed Matter*, 650:414543, 2023.

[48] Fernandes, D.M., Mathumba, P., Fernandes, A.J., Iwuoha, E.I. and Freire, C. Towards efficient oxygen reduction reaction electrocatalysts through graphene

doping. *Electrochimica Acta*, 319:72-81, 2019.

[49] Kumar, L., Chauhan, M., Boruah, P.K., Das, M.R., Hashmi, S.A. and Deka, S. Coral-shaped bifunctional $NiCo_2O_4$ nanostructure: a material for highly efficient electrochemical charge storage and electrocatalytic oxygen evolution reaction. *ACS Applied Energy Materials*, 3(7):6793-6804, 2020.

[50] Sandhiran, N., Ganapathy, S., Manoharan, Y., Ganguly, D., Kumar, M., Ramanujam, K. and Balachandran, S. CuO–NiO binary transition metal oxide nanoparticle anchored on rGO nanosheets as high-performance electrocatalyst for the oxygen reduction reaction. *Environmental Research*, 211:112992, 2022.

[51] Yu, J., Huang, T., Jiang, Z., Sun, M. and Tang, C. A hybrid material combined copper oxide with graphene for an oxygen reduction reaction in an alkaline medium. *Molecules*, 24(3):441, 2019.

[52] Park, Y., Shin, K., Lee, C., Lee, S.Y., Lee, Y.K., Kim, C.H., Cho, H.S., Henkelman, G. and Lee, H.M. Iterative redox activation promotes interfacial synergy in an Ag/Cu_xO catalyst for oxygen reduction. *Chemical Engineering Journal*, 446:136966, 2022.

[53] Putra, R.P., Samejima, Y., Nakabayashi, S., Horino, H. and Rzeznicka, I.I. Copper-based electrocatalyst derived from a copper chelate polymer for oxygen reduction reaction in alkaline solutions. *Catalysis Today*, 388:360-364, 2022.

[54] Saianand, G., Gopalan, A.I., Lee, J.C., Sathish, C.I., Gopalakrishnan, K., Unni, G.E., Shanbhag, D., Dasireddy, V.D., Yi, J., Xi, S. and Al-Muhtaseb, A.A.H. Mixed copper/copper-oxide anchored mesoporous fullerene nanohybrids as superior electrocatalysts toward oxygen reduction reaction. *Small*, 16(12):1903937, 2020.

[55] Hazarika, K.K., Yamada, Y., Matus, E.V., Kerzhentsev, M. and Bharali, P. Enhancing the electrocatalytic activity via hybridization of Cu (I/II) oxides with Co_3O_4 towards oxygen electrode reactions. *Journal of Power Sources*, 490:229511, 2021.

[56] Ni, Y., Qiao, Y., Kong, F., Li, R., Zhang, C., Kong, A. and Shan, Y. Electroactive Cu−P-coupled moieties doped in hierarchically porous carbon as efficient catalysts for the oxygen-reduction reaction. *Chemistry–An Asian Journal*, 13(21):3314-3320, 2018.